ARMY RESEARCH LABORATORY

Prediction of the Pitch-Damping Coefficients Using Sacks' Relations

by Paul Weinacht and James E. Danberg

ARL-TR-3231 **June 2004**

NOTICES

Disclaimers

The findings in this report are not to be construed as an official Department of the Army position unless so designated by other authorized documents.

Citation of manufacturer's or trade names does not constitute an official endorsement or approval of the use thereof.

Destroy this report when it is no longer needed. Do not return it to the originator.

Army Research Laboratory
Aberdeen Proving Ground, MD 21005-5066

ARL-TR-3231 **June 2004**

Prediction of the Pitch-Damping Coefficients Using Sacks' Relations

Paul Weinacht and James E. Danberg
Weapons and Materials Research Directorate, ARL

REPORT DOCUMENTATION PAGE

Form Approved
OMB No. 0704-0188

1. REPORT DATE *(DD-MM-YYYY)*	2. REPORT TYPE	3. DATES COVERED (From - To)
June 2004	Final	2001–2004

4. TITLE AND SUBTITLE
Prediction of the Pitch-Damping Coefficients Using Sacks' Relations

5a. CONTRACT NUMBER

5b. GRANT NUMBER

5c. PROGRAM ELEMENT NUMBER

6. AUTHOR(S)
Paul Weinacht and James E. Danberg

5d. PROJECT NUMBER
1L1612618AH

5e. TASK NUMBER

5f. WORK UNIT NUMBER

7. PERFORMING ORGANIZATION NAME(S) AND ADDRESS(ES)
U.S. Army Research Laboratory
ATTN: AMSRD-ARL-WM-BC
Aberdeen Proving Ground, MD 21005-5066

8. PERFORMING ORGANIZATION REPORT NUMBER
ARL-TR-3231

9. SPONSORING/MONITORING AGENCY NAME(S) AND ADDRESS(ES)

10. SPONSOR/MONITOR'S ACRONYM(S)

11. SPONSOR/MONITOR'S REPORT NUMBER(S)

12. DISTRIBUTION/AVAILABILITY STATEMENT
Approved for public release; distribution is unlimited.

13. SUPPLEMENTARY NOTES

14. ABSTRACT
Throughout its development, slender body theory has been generalized to predict a large variety of aerodynamic coefficients for a wide class of flight bodies. For most applications, slender body theory provides only a qualitative predictive capability. There is, however, a set of slender body relationships which has been previously derived by Sacks that allows the individual pitch-damping coefficients and the pitch-damping coefficient sums to be related to each other. Until recently, it has been difficult to assess the accuracy of these relationships due to the lack of high-quality pitch-damping data or the lack of a higher order theory. The current work applies a recently developed computational fluid dynamics capability for predicting all three pitch-damping coefficients. From this analysis, the accuracy of these relationships has been assessed and their engineering significance demonstrated. One important result is that the pitch-damping relations developed by Sacks allow the individual pitch-damping coefficients to be determined from the pitch-damping coefficient sum with a high degree of accuracy.

15. SUBJECT TERMS
aerodynamics, projectile flight mechanics, pitch-damping

16. SECURITY CLASSIFICATION OF:			17. LIMITATION OF ABSTRACT	18. NUMBER OF PAGES	19a. NAME OF RESPONSIBLE PERSON
a. REPORT	b. ABSTRACT	c. THIS PAGE			Paul Weinacht
UNCLASSIFIED	UNCLASSIFIED	UNCLASSIFIED	UL	40	19b. TELEPHONE NUMBER (*Include area code*) 410-278-4280

Contents

List of Figures

INTENTIONALLY LEFT BLANK.

1. Introduction

The pitch-damping moment coefficients C_{m_q} (due to body transverse angular rate) and $C_{m_{\dot{\alpha}}}$ (due to angular rate associated with angle of attack) play an important role in the performance and dynamic stability of flight bodies. The pitch-damping moment coefficient sum $C_{m_q} + C_{m_{\dot{\alpha}}}$ is of most practical importance, although the individual damping coefficients are often required in aerodynamic analyses. Throughout the past several decades, a variety of techniques and theories have been developed for predicting the pitch-damping coefficients (*1–10*). These techniques vary in their ease of use as well as their ability to accurately predict the pitch-damping coefficients.

During the course of its development, slender body theory was generalized to predict a large variety of aerodynamic coefficients including the pitch-damping coefficients (*1–2*). In general, direct application of these methods provides only qualitative results for the aerodynamic coefficients. However, elements of slender body theory have been incorporated into current engineering methods. These methods (*3–5*) have evolved considerably, although their implementation is fairly complex. Apart from implementation issues, modern engineering methods, once embodied into a computer code, are relatively easy to use and provide fast and reasonably accurate aerodynamic predictions for a large variety of flight geometries.

From slender body theory, some important relationships between the various aerodynamic coefficients can be derived, although these relationships only hold rigorously within the context of theories from which they were obtained. Bryson (*2*) derived the relatively well-known slender body result that relates the pitch-damping moment coefficient sum to the normal force coefficient, shown in equation 1:

$$C_{m_q} + C_{m_{\dot{\alpha}}} = -\left(\frac{L - x_{cg}}{D}\right)^2 C_{N_\alpha} . \tag{1}$$

Sacks (*1*), using the Blasius method for calculating the forces and moments on slender bodies from the cross-flow potential, found that many of the aerodynamic coefficients were related to each other. Sacks obtained expressions that directly related the individual pitch-damping coefficients to the normal force coefficient, such as the pitch-damping force coefficient shown in equation 2. These expressions have a form similar to Bryson's result shown in equation 1:

$$C_{N_q} = \left(\frac{L - x_{cg}}{D}\right) C_{N_\alpha} . \tag{2}$$

In practice, these relations that directly relate the damping coefficients to the normal force coefficient do not perform particularly well, even when the slender body evaluation of the

normal force coefficient is replaced with a more accurate evaluation of the normal force coefficient from sources such as experimental measurement or computational fluid dynamics (CFD) (*6*). However, these relations can be combined with empirical corrections to yield more reliable results (*6, 7*).

Sacks also found expressions that related the individual damping coefficients to each other, including the following relationship between the pitch-damping force coefficients:

$$C_{N_q} = C_{N_{\dot{\alpha}}} - C_{m_\alpha} . \tag{3}$$

Sacks' explicitly derived relation shown in equation 3 can be easily generalized using his theory to the individual pitch-damping force and moment coefficients, and the pitch-damping force and moment sums as shown in equations 4–9. For the purposes of this report, these relationships will be referred to as Sacks' relations:

$$C_{N_q} = C_{N_{\dot{\alpha}}} - C_{m_\alpha} , \tag{4}$$

$$C_{m_q} = C_{m_{\dot{\alpha}}} - C_{2m_\alpha} , \tag{5}$$

$$\left[C_{N_q} + C_{N_{\dot{\alpha}}}\right] = 2C_{N_{\dot{\alpha}}} - C_{m_\alpha} , \tag{6}$$

$$\left[C_{m_q} + C_{m_{\dot{\alpha}}}\right] = 2C_{m_{\dot{\alpha}}} - C_{2m_\alpha} , \tag{7}$$

$$\left[C_{N_q} + C_{N_{\dot{\alpha}}}\right] = 2C_{N_q} + C_{m_\alpha} , \tag{8}$$

and

$$\left[C_{m_q} + C_{m_{\dot{\alpha}}}\right] = 2C_{m_q} + C_{2m_\alpha} . \tag{9}$$

Sacks' contribution is the recognition that these relationships exist, although the same relations are implicitly contained in other theories such as that presented by Bryson (*2*).

For slender bodies, these relations are independent of configuration and are applicable to both winged and wingless bodies. The importance of these relationships is that if just one of the three pitch-damping force (or moment) coefficients can be determined (C_{N_q}, $C_{N_{\dot{\alpha}}}$ or $\left[C_{N_q} + C_{N_{\dot{\alpha}}}\right]$), the other two damping coefficients can be obtained using simple closed-form expressions. This, of course, assumes that the pitching moment coefficient C_{m_α} (first moment of the normal force) and the second moment of normal force C_{2m_α} can be obtained as well. Both of these coefficients can be obtained if the normal force distribution is known as shown in equations 10 and 11:

$$C_{m_\alpha} = \int_0^x \frac{(x_{cg} - \bar{x})}{D} \frac{dC_{N_\alpha}}{d\bar{x}} d\bar{x}, \tag{10}$$

and

$$C_{2m_\alpha} = \int_0^x \frac{(x_{cg} - \bar{x})^2}{D^2} \frac{dC_{N_\alpha}}{d\bar{x}} d\bar{x}. \tag{11}$$

Predictive methods for the static normal force and static pitching moment are well established, even for fast-design methods.

Because Sacks' relations were derived using simple approximate theories, it remains to be shown whether the validity of the relations shown in equations 4–9 exists only within the context of the theories from which they were derived or whether they are universally valid for slender bodies, or perhaps, more importantly, whether they are of general engineering significance. It is important to note that the relations shown in equations 4–9 differ somewhat from the results in equations 1 and 2 because they relate the pitch-damping coefficients to each other rather than purely to the static normal force coefficient. This suggests that Sacks' relations may more properly represent the physics compared to their counterparts which directly relate the damping coefficients to the normal force coefficient. Because of this, there is reason to investigate the validity and accuracy of Sacks' relations.

Recently, a computational approach for predicting all three of the pitch-damping coefficients has been developed (*8, 9*). The approach solves the three-dimensional (3-D) thin-layer Navier-Stokes equations for three different imposed motions that allow the three pitch-damping coefficients to be predicted independently. The pitch-damping force and moment coefficient sums are determined from the computation of a body undergoing an imposed coning motion. The individual pitch-damping coefficients are obtained from computations of a body undergoing two specific types of imposed helical motions. Each of these motions is described in the following sections. One of the key components of this method is that steady flow techniques can be employed to predict aerodynamic derivatives normally associated with time-dependent motions.

1.1 Helical Motions

Forces and moments related to the two individual rates q and $\dot{\alpha}$ can be excited independently using two types of motion where the center of gravity (CG) of the flight vehicle traverses a helical flight path. The first motion requires the vehicle's longitudinal axis to be oriented in the same direction as the center of rotation of the helix but displaced by a constant distance. Figure 1 shows a 3-D view of the motion.

This particular motion produces no rotation of the body-fixed nonrolling coordinate frame relative to an earth-fixed coordinate frame, and hence, the transverse angular velocity of the body is zero. The angle of attack and its angular rate vary continuously, producing moment

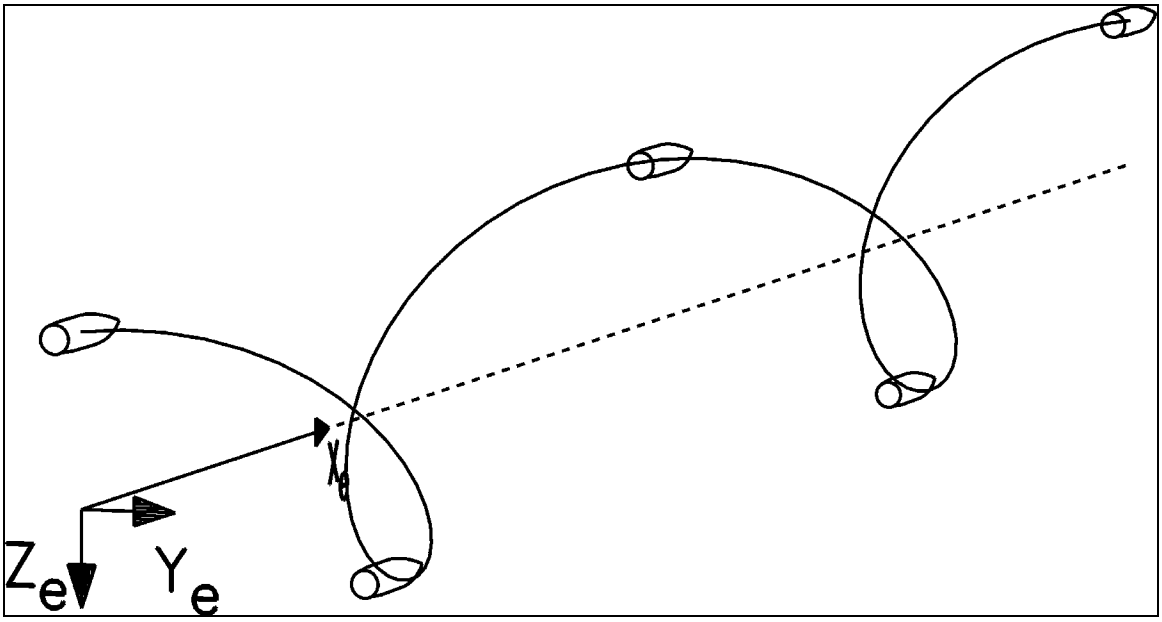

Figure 1. Helical motion with nonzero $\dot{\alpha}$ and zero q.

components associated with the coefficients C_{m_α} and $C_{m_{\dot{\alpha}}}$, respectively. This motion is referred to as "*q = 0 helical motion*" because the angular rates associated with the damping coefficient C_{m_q} are zero.

For the second motion, the longitudinal axis of the flight vehicle remains tangent to the helical flight path at each point along the trajectory. Figure 2 shows a 3-D view of this motion. The angle of attack of the incident airstream is zero because both the longitudinal axis of the body and the free-stream velocity vector are tangent to the flight path. The resulting yawing rate is also zero because the angle of attack is constant. The angular orientation of the flight body changes continuously with respect to an earth-fixed reference frame, producing a nonzero transverse angular rate.

As a result, moment components associated with the damping moment C_{m_q} are produced. This motion is referred to as "$\dot{\alpha} = 0$ *helical motion*" because the angular rates associated with the damping coefficient $C_{m_{\dot{\alpha}}}$ are zero.

For each of the helical motions, the transverse aerodynamic moment in the nonrolling frame will be periodic in time, which also indicates that the flowfield will be periodic in time when viewed from the nonrolling coordinate frame. The time dependency is removed by transforming to an orthogonal right-handed coordinate system that has its x-axis aligned with the longitudinal axis of the body and its z-axis along a line between the body's CG and the axis of rotation of the helix.

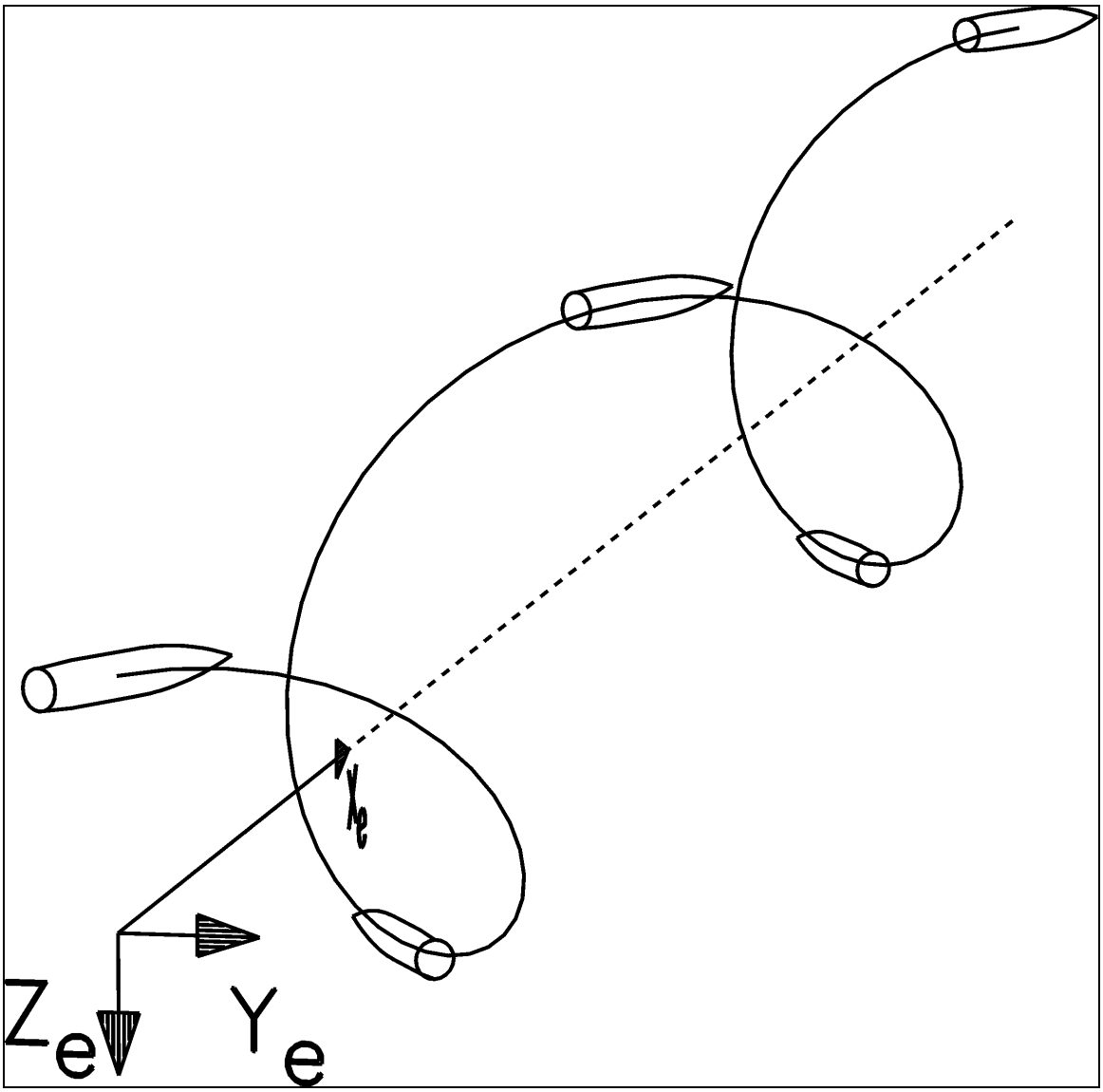

Figure 2. Helical motion with zero $\dot{\alpha}$ and nonzero q.

For each of the helical motions previously described, the spin rate of the body has not been defined. To eliminate any contributions to the aerodynamic forces and moments from the Magnus forces and moments, the spin rate is fixed to zero (see references [*8*] and [*9*] for details). The resulting in-plane moment (C_m) and side moment (C_n) coefficients in the transformed coordinate system for both type of helical motions are shown in equations 12 and 13:

$\text{Zero}-\text{spin}\, q = 0$ helical motion

$$C_m + iC_n = -C_{m_{\dot{\alpha}}}\left(\frac{\Omega D}{V}\right)\frac{R_o\Omega}{V} + iC_{m_\alpha}\frac{R_o\Omega}{V}, \tag{12}$$

$\text{Zero} - \text{spin}\ \dot{\alpha} = 0$ helical motion

$$C_m + iC_n = C_{m_q}\left(\frac{\Omega D}{V}\right)\frac{R_o \Omega}{V}. \tag{13}$$

Here, Ω is the angular velocity of the body about the helix axis, R_o is the perpendicular distance between the helix axis and the body CG, and V is the total linear velocity of the CG. Similar expressions for the individual damping force coefficients can be developed using the same approach as applied for the moment coefficients.

1.2 Coning Motion

To predict the pitch-damping coefficient sum, coning motion is employed. In steady coning motion, the longitudinal axis of the flight body performs a rotation at a constant angular velocity about a line parallel to the free-stream velocity vector and coincident with the body's CG, while oriented at a constant angle with respect to the free-stream velocity vector. This is shown schematically in figure 3. In the context of this report, coning motion also requires the CG to traverse a rectilinear path at constant velocity such that the free-stream velocity vector has a fixed orientation with the inertial frame.

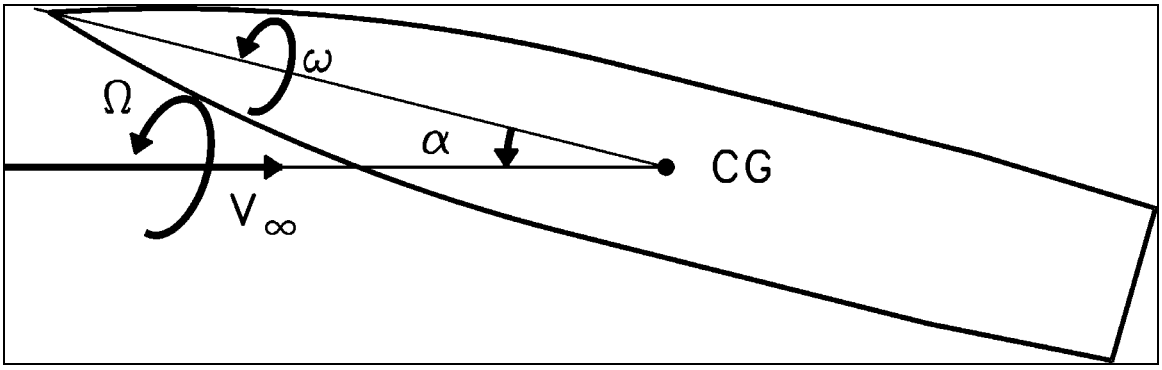

Figure 3. Schematic of coning motion.

Relative to a nonrolling coordinate frame, both the transverse angular rate of the body and the angular rate associated with the angle of attack vary in a periodic manner thereby exciting the aerodynamic forces and moments associated with both of the individual pitch-damping coefficients. Here, a specific form of coning motion, described as zero-spin coning motion, is employed. In zero-spin coning motion, the total angular velocity of the body along the longitudinal axis (the spin rate) is zero. By imposing zero spin rate on the body, the contributions from the Magnus forces and moments are eliminated.

The time dependency is removed by transforming the body-fixed nonrolling coordinate frame to an orthogonal right-handed coordinate system that has its x-axis aligned with the longitudinal axis of the body and its z-axis in the pitch-plane of the body. Within this transformed coordinate frame, in-plane moment (C_m) and side moment (C_n) coefficients have the following form:

Zero-spin coning motion

$$C_m + iC_n = i\delta\left(\frac{\Omega D}{V}\right)\left[C_{m_q} + \gamma C_{m_{\dot{\alpha}}}\right] + C_{m_\alpha}\delta \,. \tag{14}$$

Here, the side-moment is proportional to the pitch-damping moment coefficient sum and varies linearly with the coning rate Ω and sine of the total angle of attack δ. For small angles of attack, the cosine of the total angle of attack, γ, can be assumed to be one.

The pitch-damping coefficient sum can also be determined by simply adding the individual damping coefficients. In practice, there is very little difference in the two results. However, for the current study, directly predicting the pitch-damping coefficient sum using coning motion provides an alternative prediction of the pitch-damping sum and additional confirmation of the predictions of the individual coefficients.

2. Computational Technique

In the previous section, several types of steady motion were presented that produce aerodynamic forces and moments from which the various pitch-damping coefficients can be obtained. One unique feature of these motions is that they are steady. The advantage of a steady motion over an unsteady motion is that a potentially time-independent flowfield can be produced by a steady motion, permitting analysis using steady flow CFD techniques. Such techniques can be computationally less expensive than time-dependent CFD approaches. To fully exploit the steady character of the flow, special body-fixed coordinate systems have been employed to capture the steady flowfield. One feature of these coordinate frames is that they are rotating at a constant rate with respect to an inertial frame. Because of this, the governing equations of fluid motion must be modified to take into account the centrifugal and Coriolis force terms associated with the noninertial rotating frame.

The steady thin-layer Navier-Stokes equations are shown in equation 15:

$$\frac{\partial \hat{E}}{\partial \xi} + \frac{\partial \hat{F}}{\partial \eta} + \frac{\partial \hat{G}}{\partial \zeta} + \hat{H}_c + \hat{H} = \frac{1}{Re}\left(\frac{\partial \hat{S}}{\partial \zeta} + \hat{S}_c\right). \tag{15}$$

The inviscid flux vectors, $\hat{E}$, $\hat{F}$, and $\hat{G}$, the viscous term $\hat{S}$, the inviscid and viscous source terms due to the cylindrical coordinate formulation, $\hat{H}_c$ and $\hat{S}_c$, and the source term $\hat{H}$, containing the Coriolis and centrifugal force terms that result from the rotating coordinate frame, are functions of the dependent variables represented by the vector $q^T = (\rho, \rho u, \rho v, \rho w, e)$, where ρ and e are the density and the total energy per unit volume, and u, v, and w are the velocity components in axial, circumferential, and normal directions. The inviscid flux vectors and the

source term are shown in equation 16. Details of the thin-layer viscous term are available in the literature (*11*):

$$\hat{E} = \frac{1}{J}\begin{bmatrix} \rho U \\ \rho u U + \xi_x p \\ \rho v U \\ \rho w U \\ (e+p)U \end{bmatrix} \qquad \hat{F} = \frac{1}{J}\begin{bmatrix} \rho V \\ \rho u V + \eta_x p \\ \rho v V + \eta_\phi p / r \\ \rho w V + \eta_r p \\ (e+p)V \end{bmatrix}$$

$$\hat{G} = \frac{1}{J}\begin{bmatrix} \rho W \\ \rho u W + \zeta_x p \\ \rho v W + \zeta_\phi p / r \\ \rho w W + \zeta_r p \\ (e+p)W \end{bmatrix} \qquad \hat{H} = \frac{1}{J}\begin{bmatrix} 0 \\ \rho f_x \\ \rho f_\phi \\ \rho f_r \\ \rho u f_x + \rho v f_\phi + \rho w f_r \end{bmatrix}. \tag{16}$$

The pressure, p, can be related to the dependent variables by applying the ideal gas law:

$$p = (\gamma - 1)\left[e - \frac{\rho}{2}\left(u^2 + v^2 + w^2 \right) \right]. \tag{17}$$

The turbulent viscosity, μ_t, which appears in the viscous matrices, was computed using the Baldwin-Lomax turbulence model (*12*).

The Coriolis and centrifugal acceleration terms due to the rotating coordinate system, which are contained in the source term, $\hat{H}$, are shown in equation 18:

$$\vec{f} = 2\vec{\Omega} \times \vec{u} + \vec{\Omega} \times \left(\vec{\Omega} \times \vec{R} \right). \tag{18}$$

The Coriolis acceleration is a function of the angular velocity of the coordinate frame with respect to the inertial frame, $\vec{\Omega}$, and the fluid velocity vector, $\vec{u}$, which can be represented by the velocity components, u, v, and w. The centripetal acceleration is a function of the angular velocity of the rotating frame, $\vec{\Omega}$, and the displacement vector, $\vec{R}$, between the axis of rotation and the local position in the flowfield. The acceleration vector, $\vec{f}$, can be written in terms of its components along the x, ϕ, and r axes, f_x, f_ϕ, and f_r.

The steady thin-layer equations are solved using the parabolized Navier-Stokes (PNS) technique of Schiff and Steger (*11*). This "space-marching" approach integrates the governing equations from the nose of the flight body to the tail. Following the approach of Schiff and Steger, the governing equations, which have been modified here to include the Coriolis and centrifugal force terms, are solved using a conservative, approximately factored, implicit finite-difference

numerical algorithm as formulated by Beam and Warming (*13*). Details of the implementation of the source term that contains the Coriolis and centrifugal force terms are given in references (*8*) and (*9*).

The technique has been validated with available experimental data where possible, and excellent agreement is found (*8, 14*). Grid resolution studies were also performed in the original studies to ensure grid-independent solutions (*8, 9*).

3. Results

In the current context, this computational procedure allows the general applicability of Sacks' pitch-damping relations to be examined. Arguably, up to now, it has not been possible to assess the validity or accuracy of these relationships due to the uncertainty associated with experimentally derived pitch-damping data and the lack of a higher order theory. In the current research effort, the technique has been applied to two axisymmetric body geometries: an ogive-cylinder configuration and a cone-cylinder body with a flared afterbody. The accuracy of Sacks' relations is examined for each of these body geometries in supersonic flight.

3.1 Ogive-Cylinder Results

The computational approach was applied to a secant-ogive cylinder body (designated as the Army Navy Spinner Rocket [ANSR]) shown in figure 4. Results for sea-level atmospheric conditions ($\mathrm{Re}_D = 4.53 \times 10^5 M_\infty$) are shown as an example, although other Reynolds numbers and nose geometries were considered during the course of the study. Baseline results are for a flight velocity of Mach 2.5 with additional results at Mach 1.8, 3.5, and 4.5. The results presented here are representative of the other flight conditions and nose geometries examined.

For the force coefficients, the deviation or "error" in the application of Sacks' relations is defined in equation 19. The deviation Δ_1 represents the difference between the right-hand and left-hand sides of equation 4:

$$\Delta = C_{N_{\dot{\alpha}}} - C_{m_\alpha} - C_{N_q} \equiv \Delta_1 . \tag{19}$$

Note that by simple algebraic manipulations, the following relations that are algebraically equivalent to equation 19 are found:

$$\Delta = \left[C_{N_q} + C_{N_{\dot{\alpha}}}\right] - C_{m_\alpha} - 2C_{N_q} \equiv \Delta_2 , \tag{20}$$

and

$$\Delta = 2C_{N_{\dot{\alpha}}} - C_{m_\alpha} - \left[C_{N_q} + C_{N_{\dot{\alpha}}}\right] \equiv \Delta_3 . \tag{21}$$

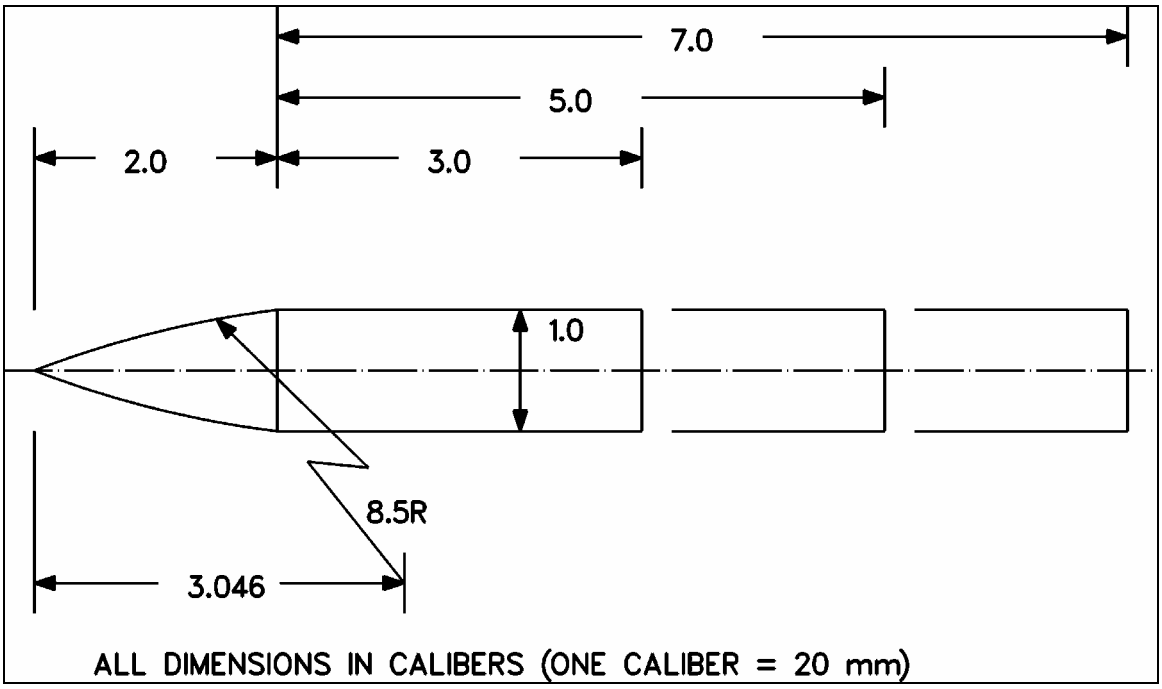

Figure 4. Schematic of ANSR configuration.

Essentially, these deviations are a measure of the accuracy of the Sacks' relations shown in equations 4, 6, and 8. It could be argued that the differences Δ_1, Δ_2, and Δ_3 are numerical errors that are not representative of physical phenomena. However, it should be noted that the deviation Δ can be computed independently in three different ways. The deviation Δ_1 is computed using the individual damping coefficients C_{N_q} and $C_{N_{\dot{\alpha}}}$ obtained independently from two different types of helical motion, while Δ_2 and Δ_3 are computed from the pitch-damping coefficient sum $C_{N_q} + C_{N_{\dot{\alpha}}}$ and one of the two individual damping coefficients C_{N_q} and $C_{N_{\dot{\alpha}}}$, respectively. The importance of having three independent methods for determining Δ is to demonstrate that the deviation is not due to an "error" in the prediction of any one of the three damping coefficients. Similar expressions for the deviation of the moment coefficients $\overline{\Delta}$ can also be obtained and are shown in equations 22–24:

$$\overline{\Delta} = C_{m_{\dot{\alpha}}} - C_{2m_\alpha} - C_{m_q} \equiv \overline{\Delta}_1, \tag{22}$$

$$\overline{\Delta} = \left[C_{m_q} + C_{m_{\dot{\alpha}}}\right] - C_{2m_\alpha} - 2C_{m_q} \equiv \overline{\Delta}_2, \tag{23}$$

and

$$\overline{\Delta} = 2C_{m_{\dot{\alpha}}} - C_{2m_\alpha} - \left[C_{m_q} + C_{m_{\dot{\alpha}}}\right] \equiv \overline{\Delta}_3. \tag{24}$$

Figure 5 shows the computed deviation for the force coefficient as a function of body length at Mach 2.5. Here, the body has been lengthened to 20 calibers to more clearly illustrate the variation of the deviation with body length. There is very good correlation between the three different methods of computing Δ, suggesting that the deviation is representative of a physical effect rather than simply numerical error. The deviation is very small over the nose and begins to grow in a linear fashion a couple of body diameters aft of the nose. The deviation (for the force) can be shown to be independent of CG position using the CG translation relations for the individual force coefficients. This was also confirmed by varying the CG position in the computations as well. The computed deviation was also found to be somewhat dependent on nose length and Mach number, although the results shown are representative of the trends observed for the other flight conditions.

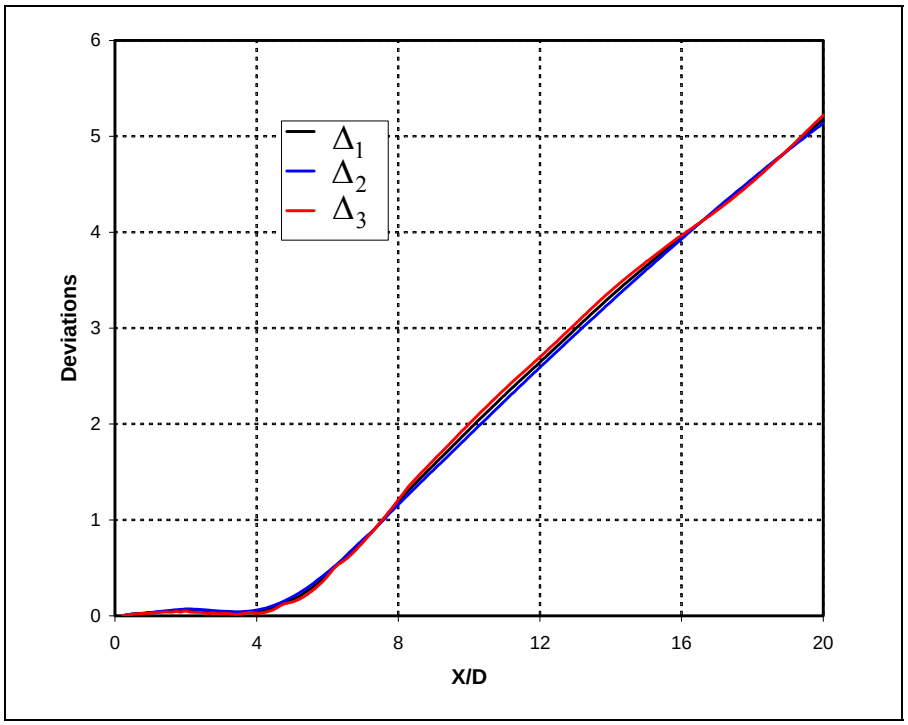

Figure 5. Comparison of the three computed deviations Δ_1, Δ_2, and Δ_3 vs. body length, ANSR, and Mach 2.5.

Figure 6 shows the computed deviations for the force, Δ_1, Δ_2, and Δ_3, compared with the individual pitch-damping coefficients and the pitch-damping sum. Relative to $C_{N_{\dot{\alpha}}}$, and the pitch-damping force sum, the deviation is quite small. The distribution of the deviation is also small compared with the pitch-damping force coefficient C_{N_q}, except near the end of the body where C_{N_q} itself is nearly zero. Equation 4 shows that according to Sacks' relation, the difference between $C_{N_{\dot{\alpha}}}$ and C_{N_q} is the pitching moment coefficient C_{m_α}. This is also graphically shown in figure 6. Near the nose of the body, the difference between the two damping coefficients, $C_{N_{\dot{\alpha}}}$ and C_{N_q}, increases at nearly the same rate as the pitching moment

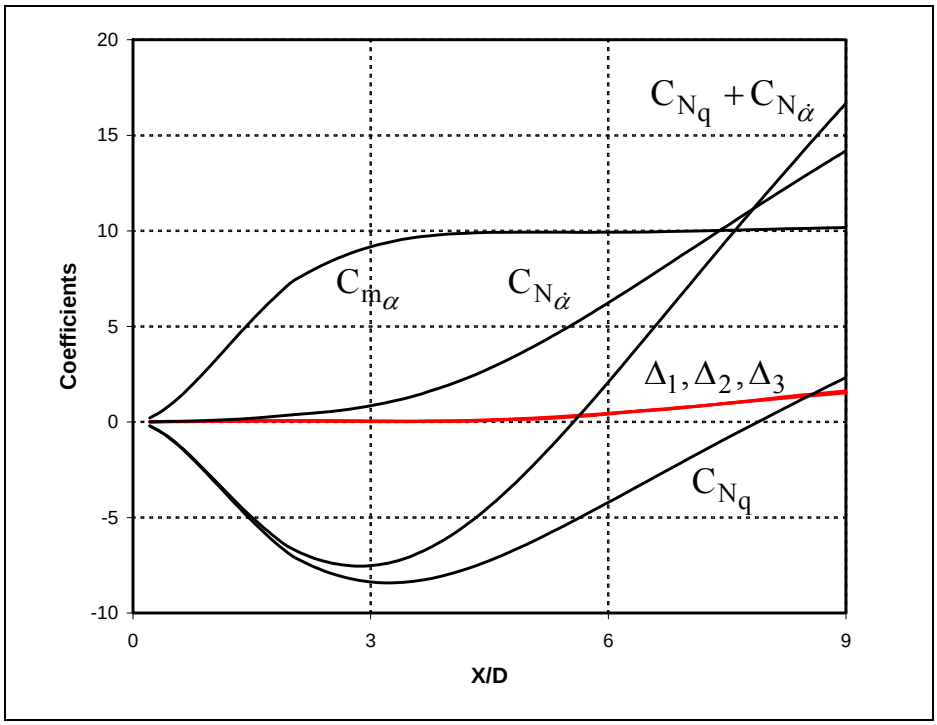

Figure 6. Comparison of the three computed deviations Δ_1, Δ_2, and Δ_3 relative to the damping force coefficients, ANSR, Mach 2.5, $x_{cg}/L = 0.5598$, and length-to-diameter (L/D) ratio = 9.

coefficient. On the aft of the body, the pitching moment coefficient is nearly constant, and the difference between $C_{N_{\dot{\alpha}}}$ and C_{N_q} becomes relatively constant.

Figure 7 shows the computed deviation for the moment relative to the three damping coefficients of interest. Again, there is very good correlation between the three methods for computing the deviation. The computed deviation is small compared to individual damping moment coefficients and to the pitch-damping moment sum. Sacks' relation for the moment (equation 5) shows that the difference between $C_{m_{\dot{\alpha}}}$ and C_{m_q} is the pitching second-moment coefficient C_{2m_α}. This also can be seen in figure 7. In a sense, figures 6 and 7 provide some measure of the expected error in applying Sacks' relations to obtain the various damping moment coefficients given that normal force distribution (or C_{m_α} and C_{2m_α}) and one of the pitch-damping coefficients is known.

The most likely application of Sacks' relations in practical situations is to compute the individual damping coefficients from the pitch-damping coefficient sum because the pitch-damping moment sum is much easier to measure. Through simple algebraic manipulations of equations 7 and 9, the following form of the Sacks' relations can be obtained:

$$C_{m_{\dot{\alpha}}} = \left(\left[C_{m_q} + C_{m_{\dot{\alpha}}} \right] + C_{2m_\alpha} \right) / 2 , \tag{25}$$

and

$$C_{m_q} = \left(\left[C_{m_q} + C_{m_{\dot{\alpha}}} \right] - C_{2m_\alpha} \right) / 2 . \tag{26}$$

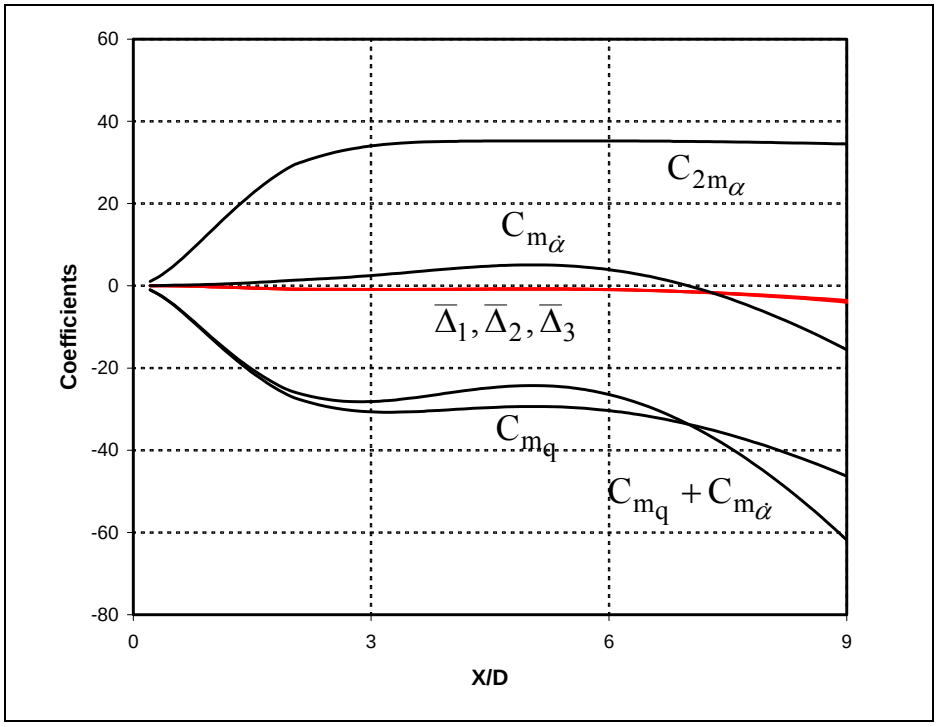

Figure 7. Comparison of the three computed deviations $\bar{\Delta}_1$, $\bar{\Delta}_2$, and $\bar{\Delta}_3$ relative to the damping moment coefficients, ANSR, Mach 2.5, $x_{cg}/L = 0.5598$, and L/D = 9.

Figure 8 shows a comparison of the pitch-damping moment coefficients C_{m_q} and $C_{m_{\dot{\alpha}}}$ obtained by applying the Sacks' relationships using the pitch-damping moment coefficient sum $\left[C_{m_q} + C_{m_{\dot{\alpha}}} \right]$ and the second-moment coefficient of the normal force C_{2m_α}. Here, CFD has been used to compute both $\left[C_{m_q} + C_{m_{\dot{\alpha}}} \right]$ and C_{2m_α}. The results from the application of these relations are compared with the CFD predictions of the individual damping coefficients. The predictions were obtained at a flight velocity of Mach 2.5. The coefficients C_{m_q} and $C_{m_{\dot{\alpha}}}$ are overpredicted and underpredicted by ~5% and 12%, respectively, although the absolute error is similar for both coefficients. The distribution of the damping coefficients over the body is also very well predicted.

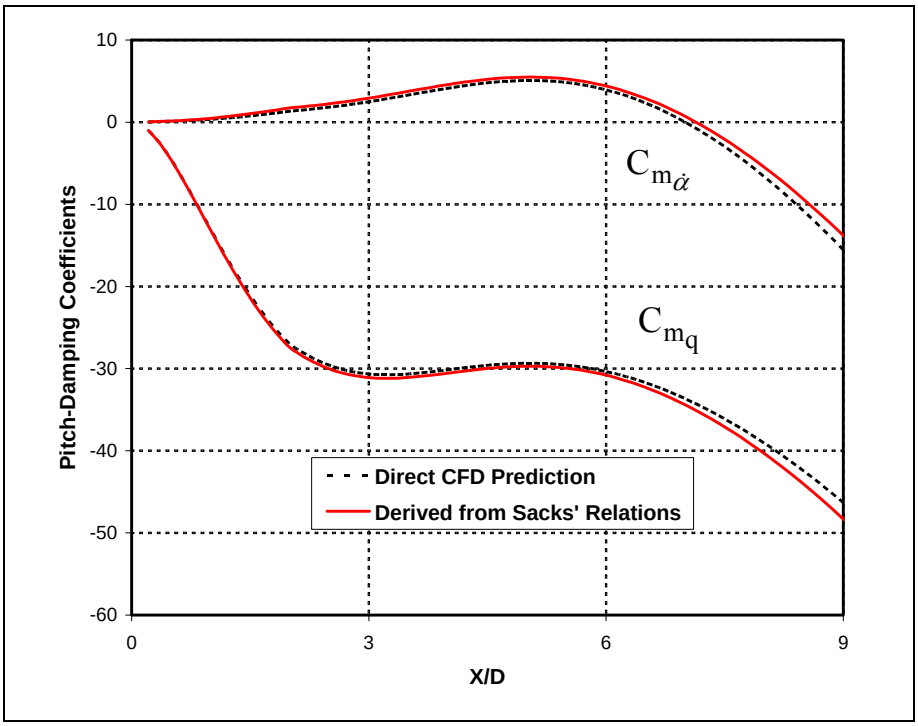

Figure 8. Comparison of the damping moment coefficients predicted from Sacks' relations with CFD predictions, ANSR, Mach 2.5, $x_{cg}/L = 0.5598$, and L/D = 9.

Figures 9–11 show similar comparisons for flight velocities of Mach 1.8, 3.5, and 4.5. The relative comparisons are very similar to the predictions at Mach 2.5 shown in figure 8. The largest Mach number effect appears to occur on the cylindrical portion of the body rather than on the nose. The relative Mach number effect, though relatively small, is captured in the application of the Sacks' relations.

Similar analysis can be performed for the force coefficients. Figure 12 shows the comparison of the individual pitch-damping moment coefficients C_{N_q} and $C_{N_{\dot{\alpha}}}$ predicted using the form of Sacks' relations in equations 27 and 28 with direct CFD predictions. The distribution of the force coefficients along the body is very well predicted using Sacks' relations:

$$C_{N_{\dot{\alpha}}} = \left(\left[C_{N_q} + C_{N_{\dot{\alpha}}} \right] + C_{m_\alpha} \right) / 2 , \tag{27}$$

and

$$C_{N_q} = \left(\left[C_{N_q} + C_{N_{\dot{\alpha}}} \right] - C_{m_\alpha} \right) / 2 . \tag{28}$$

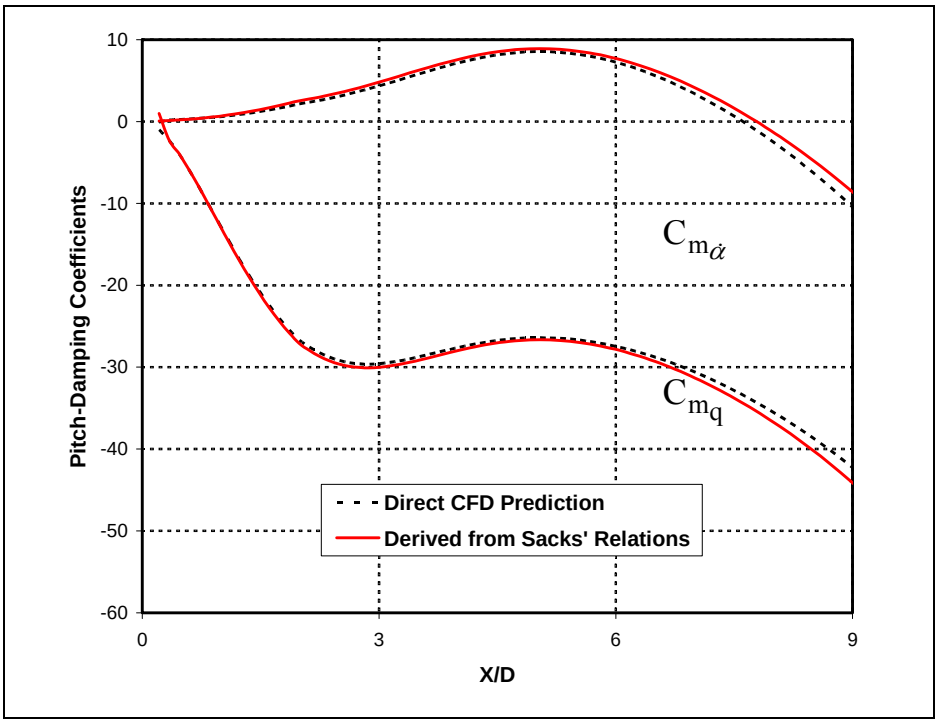

Figure 9. Comparison of the damping moment coefficients predicted from Sacks' relations with CFD predictions, ANSR, Mach 1.8, $x_{cg}/L = 0.5598$, and L/D = 9.

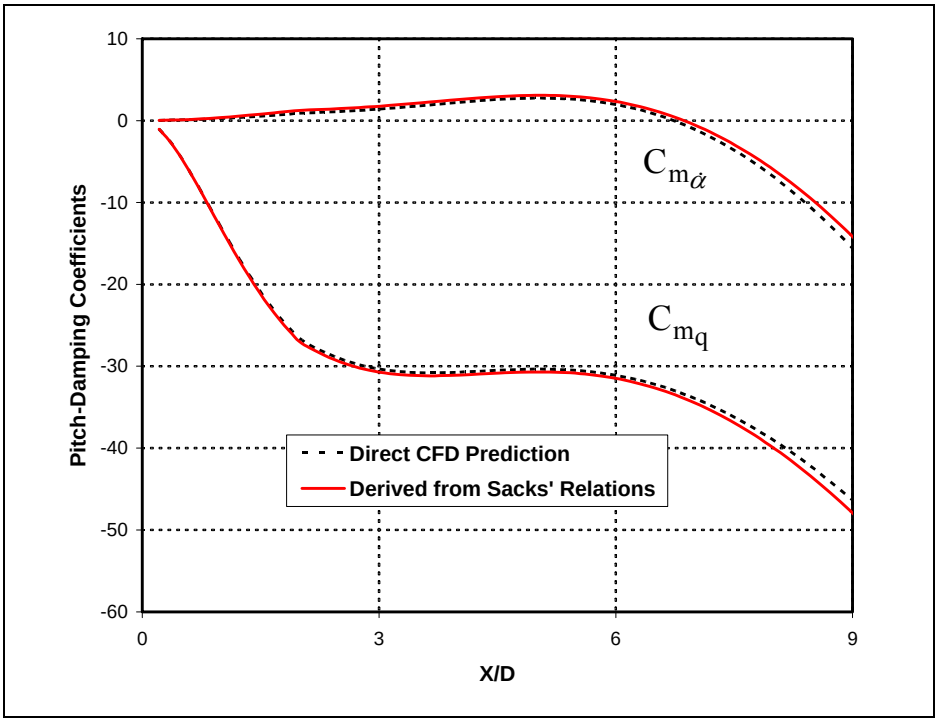

Figure 10. Comparison of the damping moment coefficients predicted from Sacks' relations with CFD predictions, ANSR, Mach 3.5, $x_{cg}/L = 0.5598$, and L/D = 9.

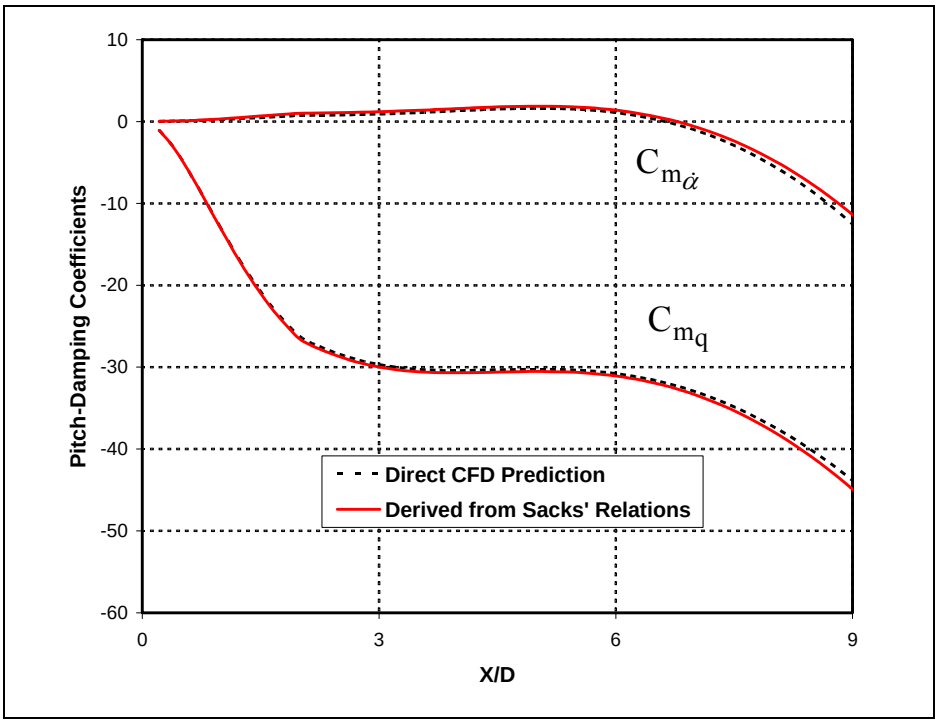

Figure 11. Comparison of the damping moment coefficients predicted from Sacks' relations with CFD predictions, ANSR, Mach 4.5, $x_{cg}/L = 0.5598$, and L/D = 9.

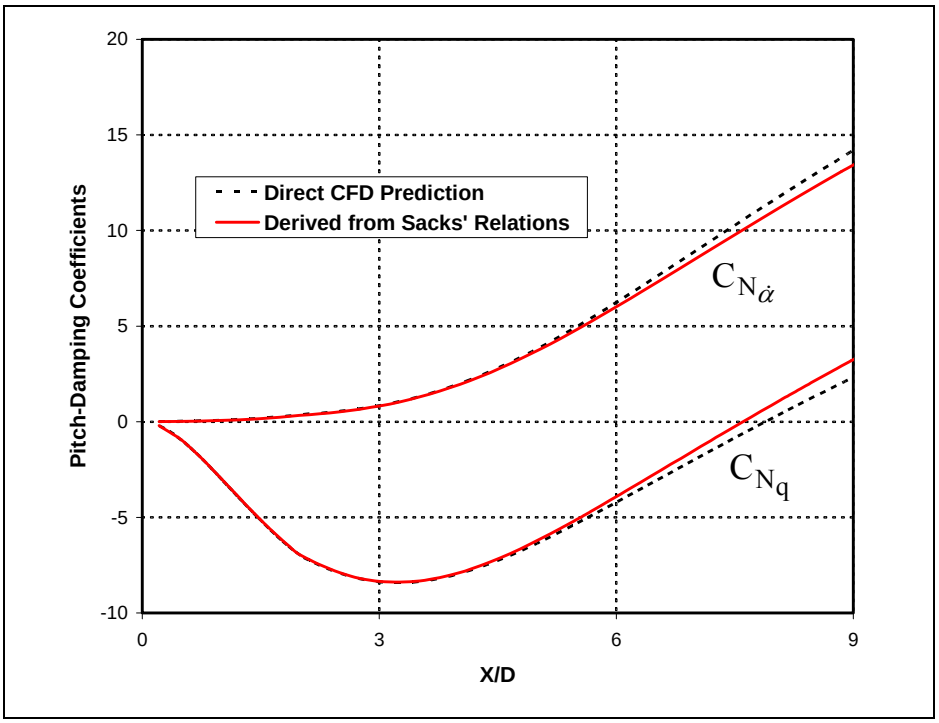

Figure 12. Comparison of the damping force coefficient predicted from Sacks' relations with CFD predictions, ANSR, Mach 2.5, $x_{cg}/L = 0.5598$, and L/D = 9.

Figure 13 shows the results for the individual pitch-damping coefficients for various CG positions for the body with the L/D ratio of 9 at Mach 2.5 obtained by applying equations 27 and 28. The results are compared with CFD results and with direct slender body theory results.

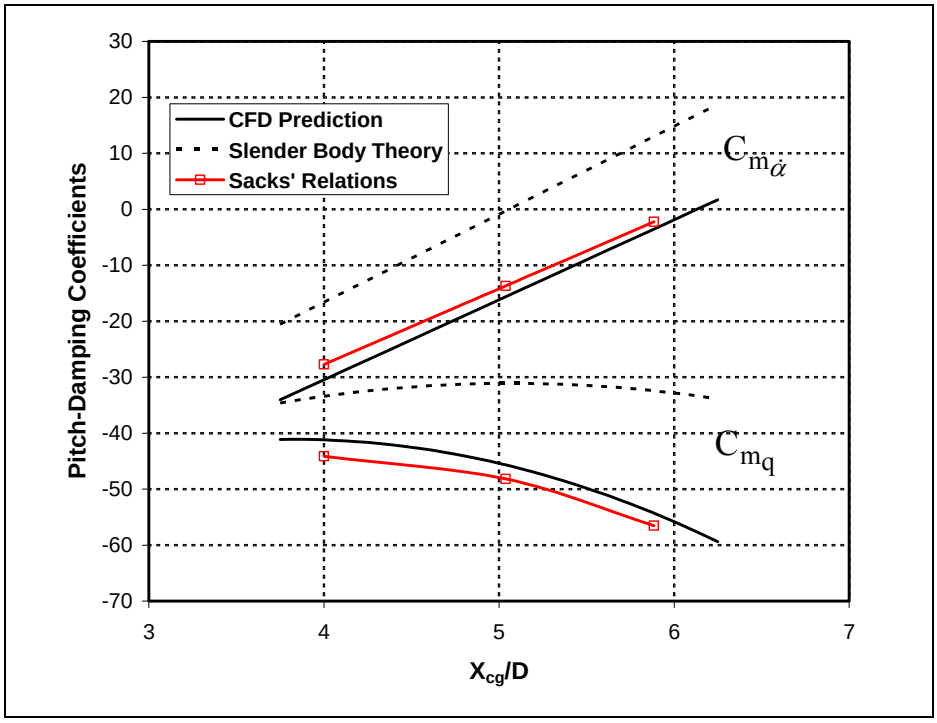

Figure 13. Comparison of the predicted damping moment coefficients with CFD and slender body theory results, ANSR, Mach 2.5, and L/D = 9.

There is very good correlation of the results obtained with Sacks' relations and the CFD results, and the results are a significant improvement over the slender body theory.

For the results shown in figures 8–12, comparisons have been made between the force and moment distributions along the body. This was done because these distributions are easily extracted from the computational results, and they allow detailed examination of the performance of Sacks' relations. It must be emphasized that it is not necessary to obtain the pitch-damping force and moment distributions in order to apply Sacks' relations because they are applicable for the global force and moment coefficients as well. This is particularly important to consider when the source of the pitch-damping coefficient data is from experiment where only global coefficients are typically available. However, Sacks' relations do require the normal force distribution to determine C_{2m_α} because generally only the normal force and pitching moment are available as global coefficients from many sources. In lieu of more sophisticated computational methods for determining the normal force distribution, fast-design aeroprediction codes (*3*) should provide acceptable accuracy for a variety of flight vehicle geometries.

To demonstrate the use of Sacks' relations when only global forces and moments are available, pitch-damping moment coefficient sum data from range firings of the ANSR have been used to estimate the individual pitch-damping moment coefficients using Sacks' relations. The normal force distribution from the fast-design aeroprediction code AP02 (*3*) has been used to predict C_{2m_α}. Figure 14 shows the predicted pitch-damping coefficients obtained from Sacks' relations using experimental measurements of the pitch-damping coefficient sum and C_{2m_α} obtained from AP02. The results are compared with direct CFD predictions of the individual damping coefficients as well as the results obtained from Sacks' relation using CFD predictions of the pitch-damping coefficient sum and C_{2m_α} shown previously in figure 10. The experimentally derived values of the individual pitch-damping coefficients compare well with the predicted results. The results also indicate that the biggest source of error is produced by the uncertainty in the experimentally derived pitch-damping moment coefficient rather than the error in Sacks' relations. (The pitch-damping data used here are from a highly regarded data set and are representative of the expected accuracy for the pitch-damping coefficient sum from range firings.)

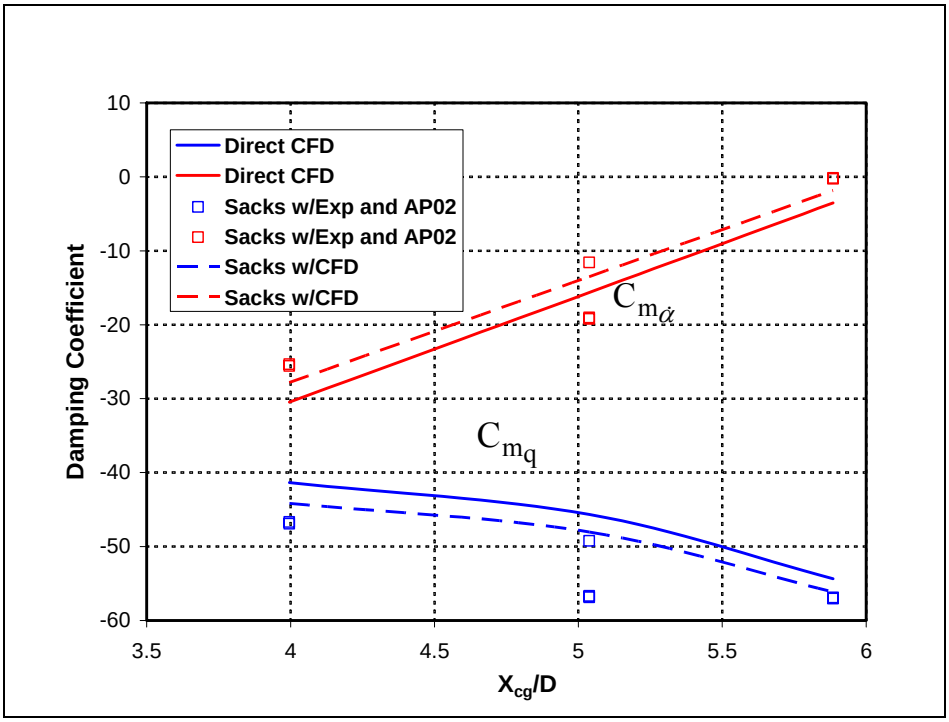

Figure 14. Comparison of the damping moment coefficients derived from experimental data or CFD using Sacks' relations with direct CFD prediction, ANSR, Mach 2.5, and L/D = 9.

Both Sacks (*1*) and Bryson (*2*) obtained relations between the pitch-damping coefficients and the normal force coefficient shown previously in equations 1 and 2. Relatively speaking, equations 1 and 2 do not perform particularly well, especially when compared to Sacks' relations

(equations 4–9). Figure 15 shows a comparison of the CFD prediction of the pitch-damping coefficient C_{N_q} with results obtained using equation 2 and Sacks' relation (equation 28). As before, CFD results were used to obtain the aerodynamic coefficients required in equations 2 and 28. The results obtained with equation 2 provide only a qualitative prediction of the distribution of C_{N_q} compared with the result obtained using Sacks' relation (equation 28), which is in much better agreement with the CFD predictions. Instead of relating the pitch-damping coefficients to the normal force coefficient as in equation 2, Sacks' relations relate the pitch-damping coefficient to each other. These results seem to imply the pitch-damping coefficients are more closely related to each other than they are to the normal force coefficient. Figure 16 shows a comparison of the pitch-damping moment coefficient sum $C_{m_q} + C_{m_{\dot{\alpha}}}$ from direct CFD prediction with the results obtained using Bryson's relation (equation 1), which like equation 2, relates the damping coefficient to the normal force coefficient. The distribution of $C_{m_q} + C_{m_{\dot{\alpha}}}$ is relatively poorly predicted compared with the CFD result, although total moment for entire configuration differs by only 25%.

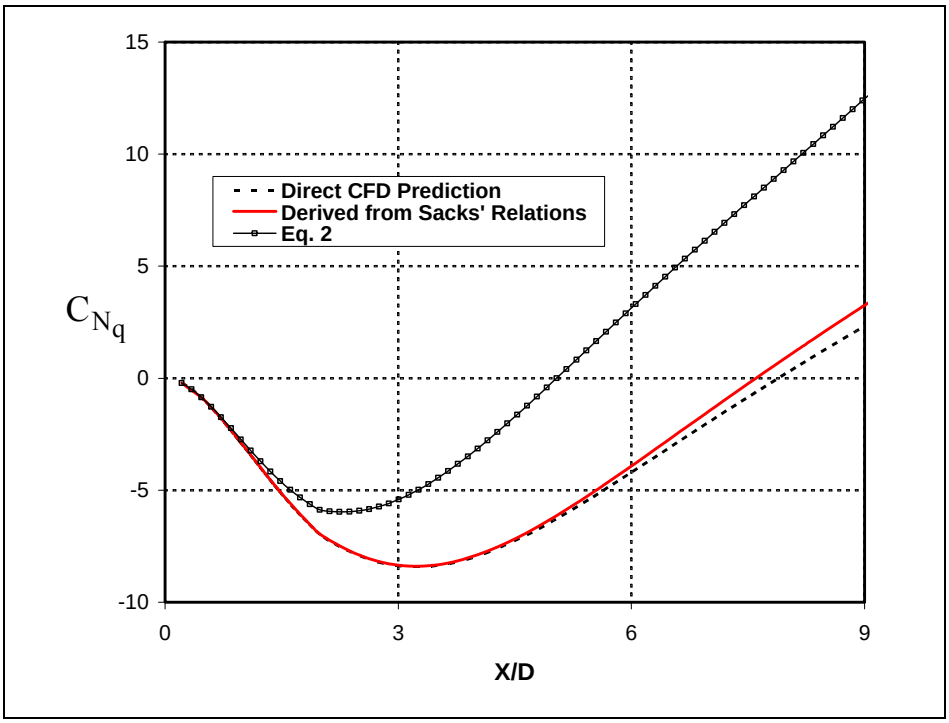

Figure 15. Comparison of the pitch-damping force coefficient C_{N_q} obtained from direction CFD predictions, predictions using Sacks' relation (equation 28) and equation 2, ANSR, Mach 2.5, $x_{cg}/L = 0.5598$, and $L/D = 9$.

3.2 Flared Projectile Results

The performance of Sacks' relations was also examined for a flared projectile geometry shown in figure 17. Predictions of the pitch-damping coefficient sum have been validated previously for

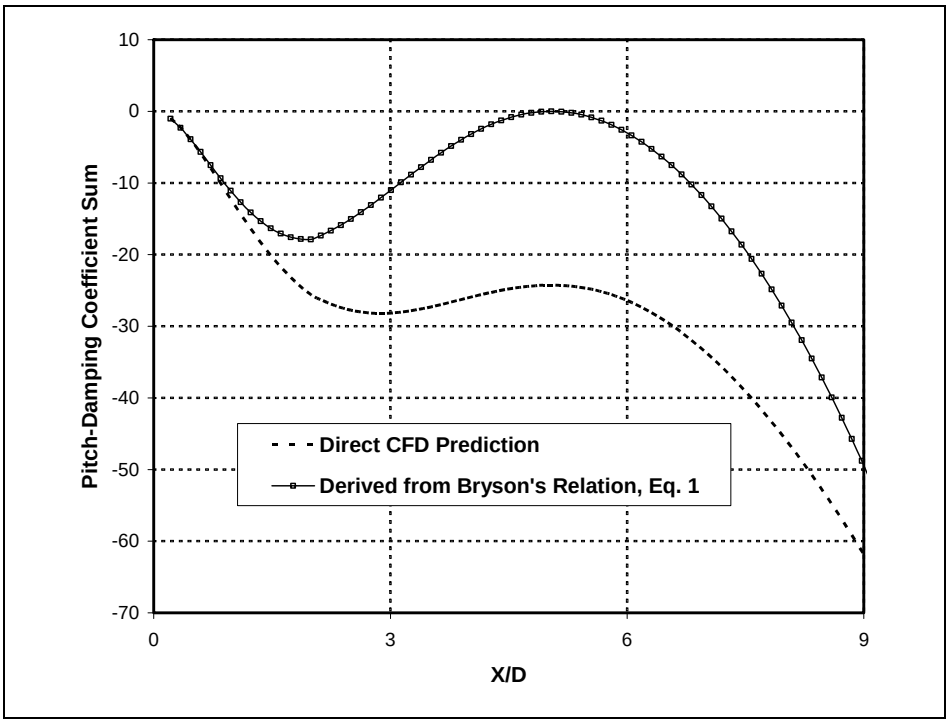

Figure 16. Comparison of the pitch-damping moment coefficient sum predicted from Bryson's relation (equation 1) with CFD predictions, ANSR, Mach 2.5, $x_{cg}/L = 0.5598$, and L/D = 9.

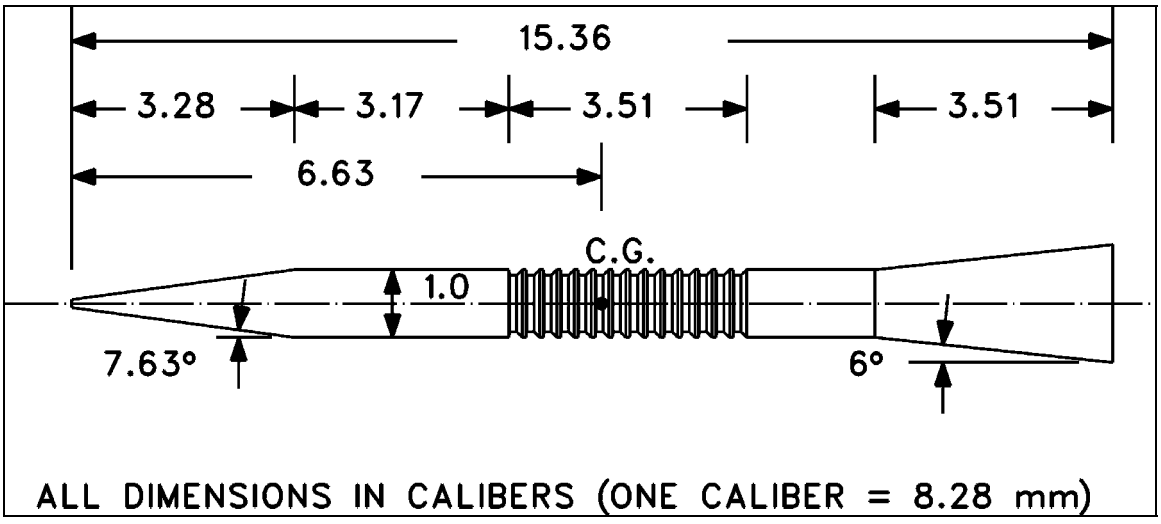

Figure 17. Schematic of the flared projectile geometry.

this configuration (*14*). For the current report, additional predictions of the individual pitch-damping coefficients were also performed for flight velocities between Mach 2 and Mach 5.

Figure 18 shows the predicted deviations of the moment compared with the individual pitch-damping coefficients at Mach 2. Again, the deviation over the body is small compared to the pitch-damping coefficients even on the afterbody where both the geometry and moment coefficients are changing significantly. Similar results were found at the other flight velocities.

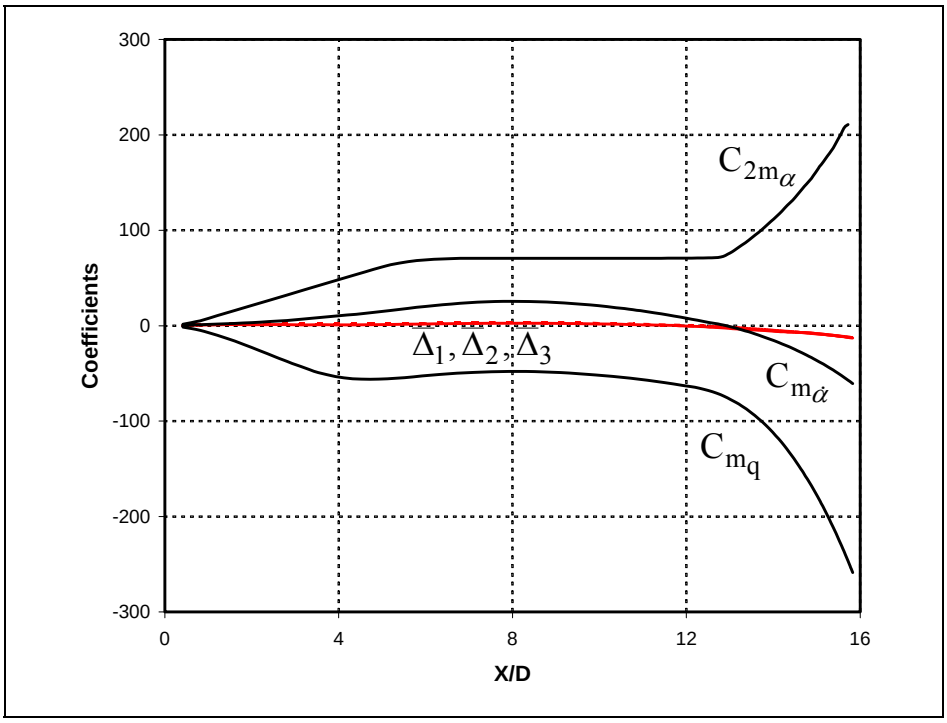

Figure 18. Comparison of the three computed deviations, $\bar{\Delta}_1$, $\bar{\Delta}_2$, and $\bar{\Delta}_3$ relative to the damping moment coefficients, flared projectile, and Mach 2.

Similar to the results for the secant ogive/cylinder configuration, the form of Sacks' relations embodied in equations 25 and 26 was applied to determine the individual pitch-damping coefficients from the pitch-damping moment coefficient sum and the pitching second-moment coefficient for the flared projectile geometry. Comparisons were made with direct CFD predictions.

Figures 19 and 20 show comparisons of the individual pitch-damping moment coefficients at Mach 2 and 5, respectively, for the flare projectile geometry. Very good agreement between the results obtained by applying Sacks' relations and direct CFD predictions are found. Additional results for the same flare projectile with the 6° flare replaced by a 15° flare were also obtained and are shown in figure 21. Despite a nearly doubling of the pitch-damping coefficient due to the larger flare, the Sacks' relations results are in very good agreement with the direct CFD predictions.

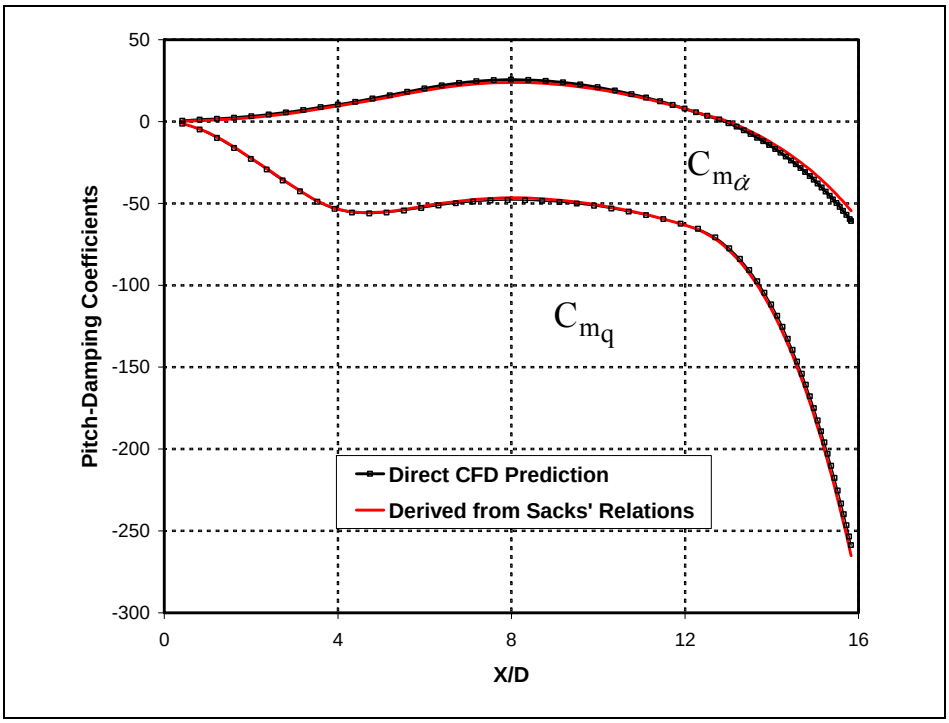

Figure 19. Comparison of the damping moment coefficient predicted from Sacks' relations with CFD predictions, flared projectile, and Mach 2.

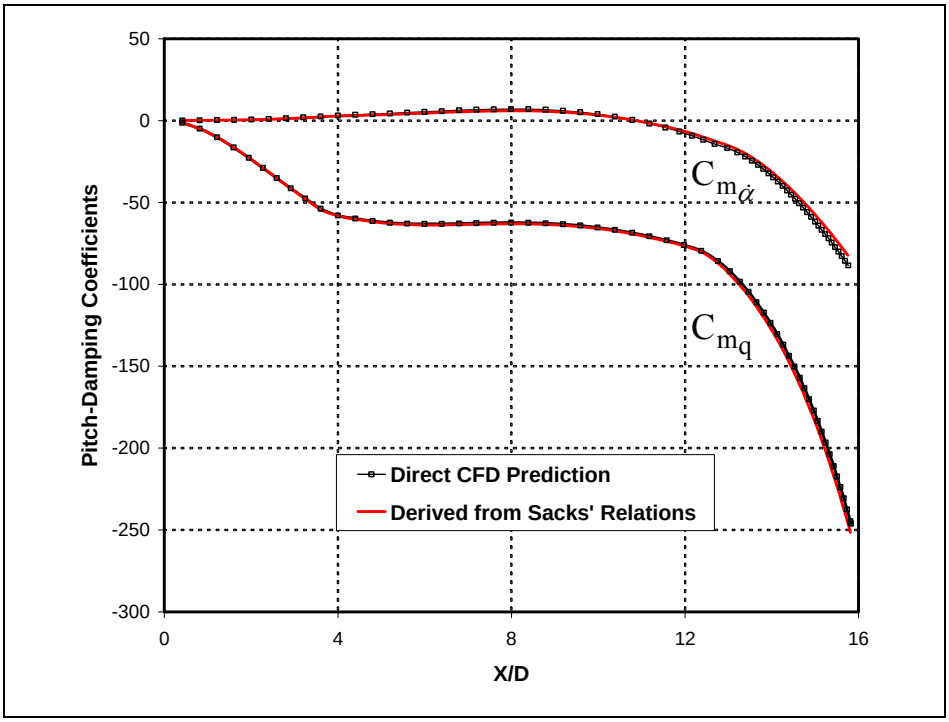

Figure 20. Comparison of the damping moment coefficient predicted from Sacks' relations with CFD predictions, flared projectile, and Mach 5.

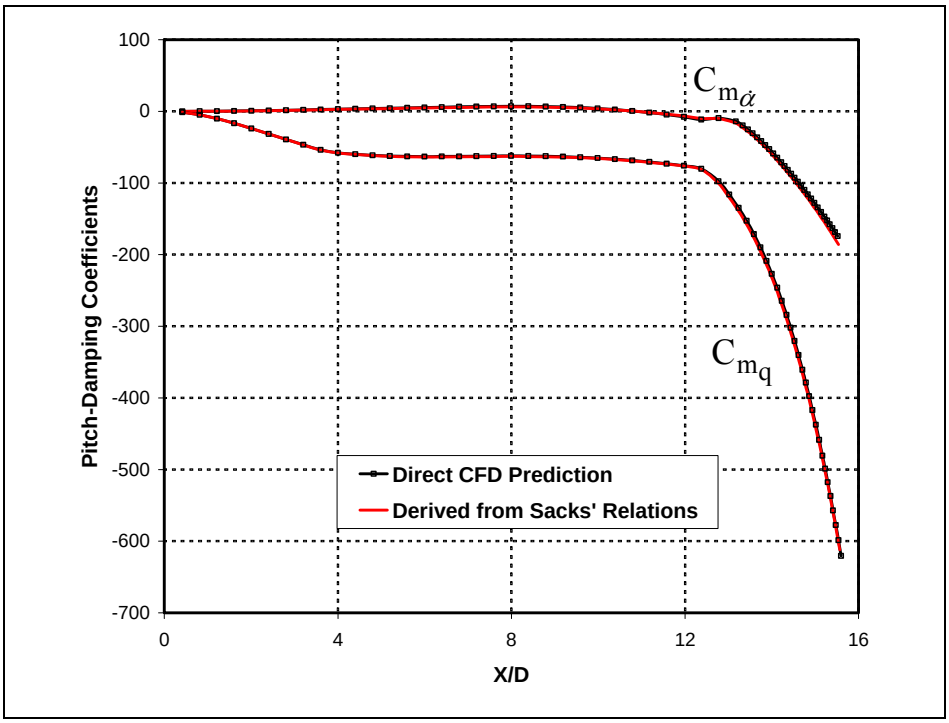

Figure 21. Comparison of the damping moment coefficient predicted from Sacks' relations with CFD predictions, 15° flared projectile, and Mach 5.

4. Summary

In conclusion, the results presented here indicate that Sacks' pitch-damping relations are only strictly valid under the context of the theory from which they were originally developed. They do, however, provide a reasonably good means of estimating the pitch-damping coefficients when one of the three pitch-damping coefficients can be determined. The most likely practical use of these relations might be to provide estimates of the individual pitch-damping coefficients using values of the pitch-damping coefficient sum determined from some other source, such as experimental data and engineering estimation approaches or when the additional expense of the separate CFD computations of the individual pitch-damping coefficients is not justified. In some cases, it appears that the error in applying these relationships is smaller than the error associated with generating the initial pitch-damping coefficient (such as with engineering estimation approaches) from which the other two damping coefficients are derived using Sacks' relations.

Applying Sacks' relations to determine the individual pitch-damping coefficients from the pitch-damping sum represents only one possible application of Sacks' relations. These relations could also benefit theoretical developments because theories for predicting the pitch-damping coefficients need only focus on a single damping coefficient. The other damping coefficients

could then be obtained from Sacks' relations. Such an approach has been already used as an estimation procedure for the damping coefficients (*6*). In this work, the distribution of $C_{N_{\dot{\alpha}}}$ along the body is predicted using slender body theory with empirically based corrections. The damping coefficient C_{N_q} can then be obtained from Sacks' relations. Once the damping force distributions are known, the damping moments can be easily obtained by integration of the force loadings. Improvements in the estimates of C_{N_q} from Sacks' relations can also be obtained by correlating the error Δ as well – an approach used in reference (*6*) to further improve the estimates of C_{N_q}.

Finally, in the currently report, only axisymmetric configurations in supersonic flight have been considered. The theory from which Sacks derived the relations considered here is applicable to both wingless and winged vehicles. Further research is still required to assess the performance of Sacks' relations for winged vehicles and for other flight velocity regimes.

5. References

1. Sacks, A. H. *Aerodynamic Forces, Moments, and Stability Derivatives for Slender Bodies of General Cross Section*; NACA Technical Note 3283; National Advisory Committee for Aeronautics: Washington, DC, November 1954; p 27.

2. Bryson, A. E., Jr. Stability Derivatives for a Slender Missile With Application to a Wing-Body-Vertical-Tail Configuration. *Journal of the Aeronautical Sciences* **May 1953**, *20* (5), 297–308.

3. Moore, F. G.; Hymer, T. C. *The 2002 Version of the Aeroprediction Code: Part I – Summary of New Theoretical Methodology*; NSWCDD/TR-01/108; Naval Surface Warfare Center: Dahlgren, VA, March 2002.

4. Vukelich, S. R.; Jenkins, J. E. *Missile DATCOM: Aerodynamic Prediction on Conventional Missiles Using Component Build-up Techniques*; AIAA Paper 84-0388; American Institute of Aeronautics and Astronautics: Reston, VA, January 1984.

5. Whyte, R. E. *Spinner – A Computer Program for Predicting the Aerodynamic Coefficients of Spin Stabilized Projectiles*; Class 2 Report No. 69APB3; General Electric Company: Burlington, VA, August 1969.

6. Danberg, J. E.; Weinacht, P. *Approximate Computation of Pitch-Damping Coefficients*; AIAA Paper 2002-5048; American Institute of Aeronautics and Astronautics: Reston, VA, August 2002.

7. Sigal, A. *Correlation of the Damping in Pitch Stability Derivatives for Body-Tail Configurations*; AIAA Paper 94-3482; American Institute of Aeronautics and Astronautics: Reston, VA, August 2002.

8. Weinacht, P.; Sturek, W. B.; Schiff, L. B. Navier-Stokes Predictions of Pitch-Damping for Axisymmetric Projectiles. *Journal of Spacecraft and Rockets* **1997**, *34* (6), 753–761.

9. Weinacht, P. Navier-Stokes Predictions of the Individual Components of the Pitch-Damping Sum. *Journal of Spacecraft and Rockets* **1998**, *35* (5), 598–605.

10. Park, S. H.; Kim, Y.; Kwon, J. H. Prediction of Damping Coefficients Using the Unsteady Euler Equations. *Journal of Spacecraft and Rockets* **2003**, *40* (3), 356–362.

11. Schiff, L. B.; Steger, J. L. Numerical Simulation of Steady Supersonic Viscous Flow. *AIAA Journal* **1980**, *18* (12), 1421–1430.

12. Baldwin, B. S.; Lomax, H. *Thin Layer Approximation and Algebraic Model for Separated Turbulent Flows*; AIAA Paper 78-257; American Institute of Aeronautics and Astronautics: Reston, VA, January 1978.

13. Beam, R.; Warming, R. F. An Implicit Factored Scheme for the Compressible Navier-Stokes Equations. *AIAA Journal* **1978**, *16* (4), 85–129.

14. Weinacht, P. *Navier-Stokes Predictions of Pitch-Damping for a Family of Flared Projectiles*; AIAA Paper 91-3339; American Institute of Aeronautics and Astronautics: Reston, VA, September 1991.

List of Symbols, Abbreviations, and Acronyms

a	Speed of sound
C_m	Pitching moment coefficient, $\frac{\overline{M}}{\frac{1}{2}\rho_\infty V^2 S_{ref} D}$
C_{m_α}	Pitching moment coefficient slope with respect to angle of attack, $\frac{\partial C_m}{\partial \alpha}$
C_{2m_α}	Pitching second moment coefficient slope with respect to angle of attack, $\frac{\partial C_{2m}}{\partial \alpha}$
$C_{m_{\dot{\alpha}}}$	Pitch-damping moment coefficient slope, $\frac{\partial C_m}{\partial\left(\frac{\dot{\alpha} D}{V}\right)}$
C_{m_q}	Pitch-damping moment coefficient slope, $\frac{\partial C_m}{\partial\left(\frac{q D}{V}\right)}$
$C_{m_q} + C_{m_{\dot{\alpha}}}$	Pitch-damping moment coefficient
C_n	Side moment coefficient
C_N	Normal force coefficient, $\frac{\overline{F}}{\frac{1}{2}\rho_\infty V^2 S_{ref}}$
C_{N_α}	Normal force coefficient slope with respect to angle of attack, $\frac{\partial C_N}{\partial \alpha}$
$C_{N_{\dot{\alpha}}}$	Pitch-damping force coefficient slope, $\frac{\partial C_N}{\partial\left(\frac{\dot{\alpha} D}{V}\right)}$
C_{N_q}	Pitch-damping force slope, $\frac{\partial C_N}{\partial\left(\frac{q D}{V}\right)}$
$C_{N_q} + C_{N_{\dot{\alpha}}}$	Pitch-damping force coefficient

D	Reference diameter
e	Total energy per unit volume
$\hat{E}, \hat{F}, \hat{G}$	Flux vectors in transformed coordinates
$\overline{F}$	Force
$\hat{H}$	Source term in Navier-Stokes equations due to rotating coordinate frame
$\hat{H}_c$	Source term in Navier-Stokes equations due to cylindrical coordinate formulation
L	Body length
M	Mach number
$\overline{M}$	Moment
p	Pressure
q	Transverse angular rate of body as used in flight mechanics equations
q^T	Transposed vector of dependent variables as used in Navier-Stokes equations
r	Radial coordinate
Re	Reynolds number, $a_\infty \rho_\infty D / \mu_\infty$
R_o	Helix radius
S_{ref}	Reference area, $S_{ref} = \frac{\pi D^2}{4}$
$\hat{S}$	Viscous flux vector
$\hat{S}_c$	Viscous terms due to cylindrical coordinate formulation
u, v, w	Velocity components in the x, ϕ, r directions
U, V, W	Contravariant velocity components
V	Freestream velocity
X_e, Y_e, Z_e	Earth-fixed coordinates
x	Axial location along body from nose
$\overline{x}$	Integration variable associated with axial location along body from nose
x_{cg}	Axial location of center of gravity from nose

Greek Symbols

α	Angle of attack
$\dot{\alpha}$	Angular rate associated with angle of attack
β	Yaw angle
γ	Cosine of total angle of attack
δ	Sine of total angle of attack
Δ	Deviation or error in Sacks' relations for force
$\overline{\Delta}$	Deviation or error in Sacks' relations for moment
μ	Viscosity
ξ, η, ζ	Transformed coordinates in the Navier-Stokes equations
ρ	Density
ϕ	Circumferential coordinate
ω	Angular velocity about longitudinal axis
Ω	Angular rate associated with coning and helical motions

Subscripts

∞	Quantity evaluated at freestream conditions

NO. OF COPIES ORGANIZATION

1 (PDF Only) DEFENSE TECHNICAL INFORMATION CTR
DTIC OCA
8725 JOHN J KINGMAN RD
STE 0944
FT BELVOIR VA 22060-6218

1 COMMANDING GENERAL
US ARMY MATERIEL CMD
AMCRDA TF
5001 EISENHOWER AVE
ALEXANDRIA VA 22333-0001

1 INST FOR ADVNCD TCHNLGY
THE UNIV OF TEXAS
AT AUSTIN
3925 W BRAKER LN STE 400
AUSTIN TX 78759-5316

1 US MILITARY ACADEMY
MATH SCI CTR EXCELLENCE
MADN MATH
THAYER HALL
WEST POINT NY 10996-1786

1 DIRECTOR
US ARMY RESEARCH LAB
AMSRD ARL CS IS R
2800 POWDER MILL RD
ADELPHI MD 20783-1197

3 DIRECTOR
US ARMY RESEARCH LAB
AMSRD ARL CI OK TL
2800 POWDER MILL RD
ADELPHI MD 20783-1197

3 DIRECTOR
US ARMY RESEARCH LAB
AMSRD ARL CS IS T
2800 POWDER MILL RD
ADELPHI MD 20783-1197

NO. OF COPIES ORGANIZATION

ABERDEEN PROVING GROUND

1 DIR USARL
AMSRD ARL CI OK TP (BLDG 4600)

NO. OF COPIES	ORGANIZATION
1	ARROW TECH ASSOC W HATHAWAY 1233 SHELBURNE RD D-8 SOUTH BURLINGTON VT 05403
1	OREGON STATE UNIV M COSTELLO DEPT OF MECH ENGRNG CORVALLIS OR 97331
1	ATK R DOHRN MN07 LW54 4700 NATHAN LANE N PLYMOUTH MN 55442
1	AEROPREDICTION INC DR F MOORE 9449 GROVER DRIVE SUITE 201 KING GEORGE VA 22485
1	UNIV OF DELAWARE DEPT OF MECH ENGRNG TSU WEI CHU 126 SPENCER LAB NEWARK DE 19716-3140
1	COMMANDER ARDEC AMSTR AR FSF X W TOLEDO BLDG 95 SOUTH PICATINNY ARSENAL NJ 07806-5000
1	US ARMY AMRDEC AMSAM RD SS AT R W KRETZSCHMAR BLDG 5400 REDSTONE ARSENAL AL 35898-5000
1	US ARMY AMRDEC AMSAM RD SS AT M E VAUGHN BLDG 5400 REDSTONE ARSENAL AL 35898-5000
1	DYNETICS INC M S MILLER PO BOX 5500 HUNTSVILLE AL 35814-5500

NO. OF COPIES	ORGANIZATION
ABERDEEN PROVING GROUND	
24	DIR USARL AMSRD ARL WM B A HORST AMSRD ARL WM BA D LYON AMSRD ARL WM BC M BUNDY G COOPER J DESPIRITO J GARNER B GUIDOS K HEAVEY J NEWILL P PLOSTINS J SAHU S SILTON D WEBB P WEINACHT (8 CPS) A ZIELINSKI AMSRD ARL WM BD B FORCH AMSRD ARL WM BF S WILKERSON

NO. OF COPIES	ORGANIZATION
1	TECHNION ISRAEL INST OF TECH A SIGAL TECHNION CITY HAIFA 32000 ISRAEL